Active Control of Energy Transfer in Plasmonic Nanorod-Polyaniline Hybrids

Annette Jones[1], Emily K. Searles[1], Martin Mayer[2], Marisa Hoffmann[2], Niklas Gross[1], Hyuncheol Oh[1], Andreas Fery[2], Stephan Link*[1,3,4], Christy F. Landes*[1,3,4,5]

[1]*Department of Chemistry, Rice University, 6100 Main Street, Houston, Texas 77005, United States*

[2]*Leibniz-Institut für Polymerforschung Dresden e.V., Institute of Physical Chemistry and Polymer Physics, Dresden, Germany*

[3]*Smalley-Curl Institute, Rice University, 6100 Main Street, Houston, Texas 77005, United States*

[4]*Department of Electrical and Computer Engineering, Rice University, 6100 Main Street, Houston, Texas 77005, United States*

[5]*Department of Chemical and Biomolecular Engineering, Rice University, 6100 Main Street, Houston, Texas 77005, United States*

KEYWORDS: Gold nanoparticles, Nanoparticle-polymer composites, Localized surface plasmon resonance, Chemical interface damping, Single-particle spectroscopy

*To whom correspondence should be addressed: cflandes@rice.edu; slink@rice.edu

Abstract

The hybridization of plasmonic energy and charge donors with polymeric acceptors is a possible means to overcome fast internal relaxation that limits potential photocatalysis applications for plasmonic nanomaterials. Polyaniline (PANI) readily hybridizes onto gold nanorods (AuNRs) and has been used for sensitive monitoring of local refractive index changes. Here, we use single-particle spectroscopy to quantify a previously unreported plasmon damping mechanism in AuNR-PANI hybrids while actively tuning the PANI chemical structure. By eliminating contributions from heterogeneous linewidth broadening and refractive index changes, we identify efficient resonance energy transfer (RET) between AuNRs and PANI. We find that RET dominates the optical response in our AuNR-PANI hybrids during the dynamic tuning of the spectral overlap of the AuNR donor and PANI acceptor. Harnessing RET between plasmonic nanomaterials and an affordable and processable polymer such as PANI offers an alternate mechanism towards efficient photocatalysis with plasmonic nanoparticle antennas.

TOC Graphic

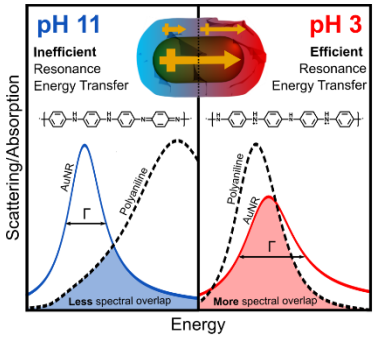

When excited with incident light, metal nanoparticles support localized surface plasmon resonances.[1-3] The plasmon is sensitive to changes in particle morphology and local environment,[4-7] providing dynamic optical insight into particle growth[8-10] and dissolution,[11-13] changes in local refractive index,[14-16] and charge [17-20] or energy transfer.[21-24] The energy available due to the plasmon's high absorption cross-section can be used in photocatalysis and photovoltaics to increase device efficiencies.[1, 25-28] Hybridization of nanoparticles with acceptors offers a way to capture the charge or energy stored by the plasmon before ultrafast relaxation of electron-hole pairs occurs.[29-32] Understanding the mechanisms of interfacial charge and energy transfer in hybrid materials is therefore crucial for future optimized device implementations.[33-36]

Charge transfer (CT) is one viable mechanism for hybrid materials, but this process requires strict band alignment and is usually restricted to hard metal-inorganic interfaces.[17, 31, 37] More important for eventual applications is that CT requires a scavenger to avoid charge imbalance, which leads to eventual decomposition and device degradation.[38-39] On the other hand, energy transfer offers an avenue for the use of soft polymers at plasmonic interfaces while relaxing the band alignment requirement and allowing for increased processability of metal-organic interfaces.[21-23, 29, 33, 40-41] Resonance energy transfer (RET) is achieved by dipole-dipole coupling between the plasmon and acceptor, generating an electron-hole pair in the acceptor itself. The creation of an electron-hole pair in the acceptor eliminates the possibility of charge accumulation on the metal.[21, 24, 40, 42-43] Efficient RET occurs when the polymer acceptor is within the decay length of the plasmon's electric field and is most efficient when the spectral overlap between the plasmon donor and polymer acceptor is greatest.[22, 44-47]

Here, we use gold nanorod (AuNR)-polyaniline (PANI) hybrids to demonstrate RET and its dynamic control by manipulating the degree of spectral overlap. Because of its reversible and controllable spectral modulation, PANI is a promising acceptor to couple with a plasmonic donor while providing ease of incorporation into existing platforms.[29, 41, 48-50] Single-particle spectroscopy provides insight into changes to the scattering of single-AuNR-PANI hybrids by monitoring the plasmon resonance energy

(E_{res}) and linewidth (Γ) without the presence of ensemble averaging inherent to bulk measurements. By monitoring changes to the single-particle Γ, RET efficiency (η_{RET}) can be determined, thereby showing how AuNR-PANI hybrids can be used to control the dynamic tuning of optical and electronic properties at soft interfaces.[24, 31, 51-54] In this study, the single-particle Γ reports on changes in RET in AuNR-PANI hybrids as the protonation state of PANI is switched by pH. Correlated plasmon spectra of AuNR-PANI hybrids are captured in both acidic and basic conditions using a fluidic cell on an inverted hyperspectral dark-field microscope. The inherent structural heterogeneity within an ensemble of AuNR-PANI hybrids is the key to being able to observe a distribution of η_{RET} that corresponds with a range of spectral overlaps.

Ensemble extinction spectra of AuNRs before and after AuNR-PANI hybridization are shown in Figure 1A. The bare AuNRs (average dimensions of 14 x 41 nm) have an ensemble longitudinal E_{res} of 1.73 eV. The formation of AuNR-PANI hybrids, with a representative transmission electron microscopy (TEM) image in the inset of Figure 1A, results in a shift in the E_{res}

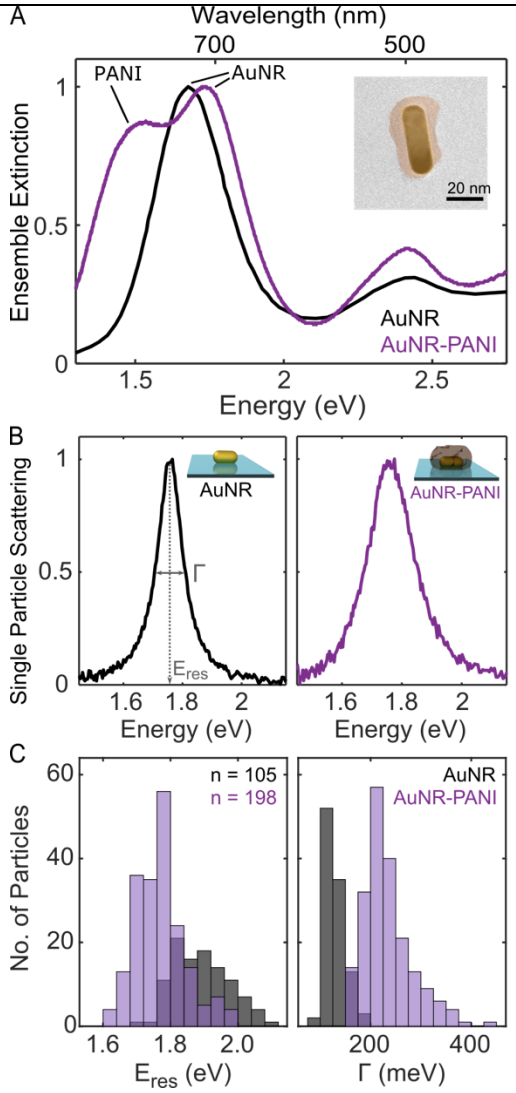

Figure 1: Upon PANI hybridization, the E_{res} decreases due to an increase in the refractive index. Single-particle spectroscopy removes inter-particle heterogeneity and PANI absorption uncovering strong damping of the plasmon Γ. A) Bulk extinction spectra of bare AuNRs and AuNR-PANI hybrids. The extinction measurements were collected using the as synthesized AuNRs and pH adjusted AuNR-PANI hybrids in solution of pH 3. Inset: TEM micrograph of a AuNR-PANI hybrid. B) Single-particle spectrum of a bare AuNR (left, black) and a AuNR-PANI hybrid (right, purple). Inset: Schematic representation of measured system. C) Histograms of AuNR (black, n=105) and AuNR-PANI hybrid (purple, n=198) E_{res}, left. Histograms of AuNR and AuNR-PANI hybrid Γ, right. These DFS measurements were carried out in air and not in a flow cell.

to higher energy, reflected at ~1.8 eV. The AuNR-PANI hybrid extinction shift confirms the successful functionalization of the AuNRs with a PANI shell, as an increase in E_{res} has been seen previously by Wang and coworkers upon PANI functionalization in the oxidative solution environment.[55] The resonance in the extinction spectrum at a lower energy than the plasmon at ~1.4 eV is from PANI absorption due to transitions from the highest occupied molecular orbital (HOMO) on the benzenoid to the lowest unoccupied molecular orbital (LUMO) on the quinoid rings.[56-57]

Single-particle analysis resolves inter-particle heterogeneity and reveals broadening of the Γ, which is not consistent with a simple refractive index change. Single-particle dark-field scattering (DFS) spectra of a representative AuNR and a AuNR-PANI hybrid with similar E_{res} reveal that the addition of a ~5 nm PANI shell drastically changes the optical response, Figure 1B. See experimental methods for a description of the single-particle measurements. The single-particle E_{res} and Γ are free from heterogeneous broadening that is present in the bulk measurements. With homogeneously broadened single-particle DFS spectra, changes to the E_{res} are directly related to changes in the local refractive index, and changes in the homogenous Γ are directly related to changes in the plasmon dephasing time.[24, 58-59] The single-particle homogeneous Γ is inversely proportional to the plasmon decay time constant, allowing change to the extent of plasmon damping to be monitored through changes to the Γ observable.[23, 31, 60] Single-particle distributions in E_{res} in the left panel of Figure 1C are consistent with previously reported changes to the AuNR-PANI hybrid measured in air, in which the addition of a 5 nm PANI shell decreased the E_{res} of the hybrid.[61-62]

Broadening of the Γ confirms that an additional relaxation pathway is opened when AuNRs are hybridized with PANI shells (Figure 1C, right). Because the Γ is inversely proportional to the plasmon dephasing time, [31-32, 51] single-particle DFS spectra can directly monitor the effects of interfacial changes on the relaxation dynamics in each AuNR. In these particles, the increase in the Γ of the AuNR-PANI hybrids when compared to bare AuNRs, Figure 1C (right), indicates the presence of an additional plasmon damping pathway. If the change in the Γ were related solely to the decrease in E_{res} due to

refractive index changes, the Γ would decrease (rather than increase) as the AuNR E_{res} shifts away from interband damping contributions.

The total single-particle Γ (Γ_{Total}) includes contributions from bulk damping (Γ_{Bulk}) intrinsic to the Au metal, and size-dependent radiation damping (Γ_{Rad}) and electron-surface scattering (Γ_{Surf}).[60, 63] Additional damping mechanisms that broaden the Γ include CT and RET and are often referred to as chemical interface damping (CID).[64] Broadening due to these additional plasmon damping pathways is represented as Γ_{CID} here. Using the average size of the AuNRs, 14 x 41 nm, the damping contributions from Γ_{Bulk}, $\Gamma_{Rad,}$ and Γ_{Surf} were removed from the Γ_{Total} of the bare AuNRs and AuNR-PANI hybrids. Damping from Γ_{Bulk} is energy-dependent due to the contributions from intraband and interband transitions intrinsic to gold and were removed using the experimental dielectric function discussed further in Figure S1. As shown in Figure S1, after the removal of the non-CID contributions the bare AuNRs have an average Γ of 16 ± 19 meV, demonstrating that these contributions alone account well for the Γ_{Total}. However, the average value for AuNR-PANI hybrids, after accounting for Γ_{Bulk}, $\Gamma_{Rad,}$ and Γ_{Surf}, is still 140 ± 50 meV, confirming that a large portion of the homogenous Γ must be attributed to Γ_{CID}. In fact, we calculate a CID efficiency of 58% (Figure S1). The increase in plasmon damping after the addition of the PANI shell is therefore attributed to CID. To assign CID to RET (as opposed to CT or other mechanisms), an additional control variable is necessary, as discussed next.

Dynamic switching of spectral overlap between donor and acceptor is used as the important control variable and achieved through modulation of PANI's protonation state, shifting PANI absorption as the polymer is tuned from emeraldine base to emeraldine salt (Figure 2). Changing the pH modulates PANI's protonation state, which in turn results in shifts in the PANI extinction maximum as shown in Figure 2A. The extinction is dominated by absorption and the change in its maximum is a result of the change in the HOMO and LUMO levels as the polymer is protonated.[54, 62] The chemical structures in Figure 2B depict protonation states of PANI in the emeraldine base and emeraldine salt form, for high and low pH environments, respectively. *In situ* modulation of PANI absorption provides dynamic control of the spectral overlap between the AuNR donor and PANI acceptor for the anticipated modulation of CID, which we hypothesize here and demonstrate below is due to RET.

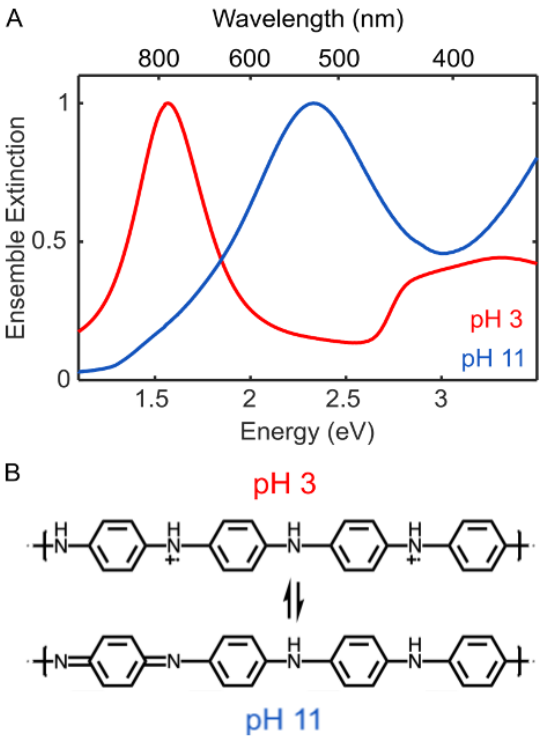

Figure 2: Increased protonation induces shifts in polymer absorption as the PANI is doped from emeraldine base to emeraldine salt. A) Normalized ensemble extinction spectra of PANI supernatant in solution extracted after hybrid synthesis at pH 3 (red) and 11 (blue). B) Chemical structures depict protonation states of PANI at high and low pH, corresponding to emeraldine base and emeraldine salt, respectively. The emeraldine salt has a positive charge and unpaired electrons on the nitrogen atom by protonation under the acidic condition.

Single-particle hyperspectral DFS allows reversible *in situ* monitoring of the E_{res} and Γ from single-AuNR-PANI hybrids in a microfluidic cell (Figure 3). A pressure-sealed optically transparent microfluidic cell is coupled with an inverted hyperspectral dark-field microscope (see experimental methods) to collect single-particle scattering spectra, Figure 3A. The environmental conditions are exchanged using syringe pumps while the sample remains on the microscope, allowing the comparison of spectral changes for the same particle under different pH conditions. Comparison of the same AuNR-PANI hybrid allows interparticle heterogeneity such as the thickness of the PANI to be removed from consideration. Reversible modulation of the spectral shape for a single-AuNR-PANI hybrid is shown in Figure 3B as the environment is changed from acidic (red, pH: 3) to basic (blue, pH: 11), and back to acidic (light red, pH: 3), demonstrated for additional AuNR-PANI hybrids in Figure S2. Even though the Γ does not return to the same value in both acidic conditions, likely due to polymer reorganization

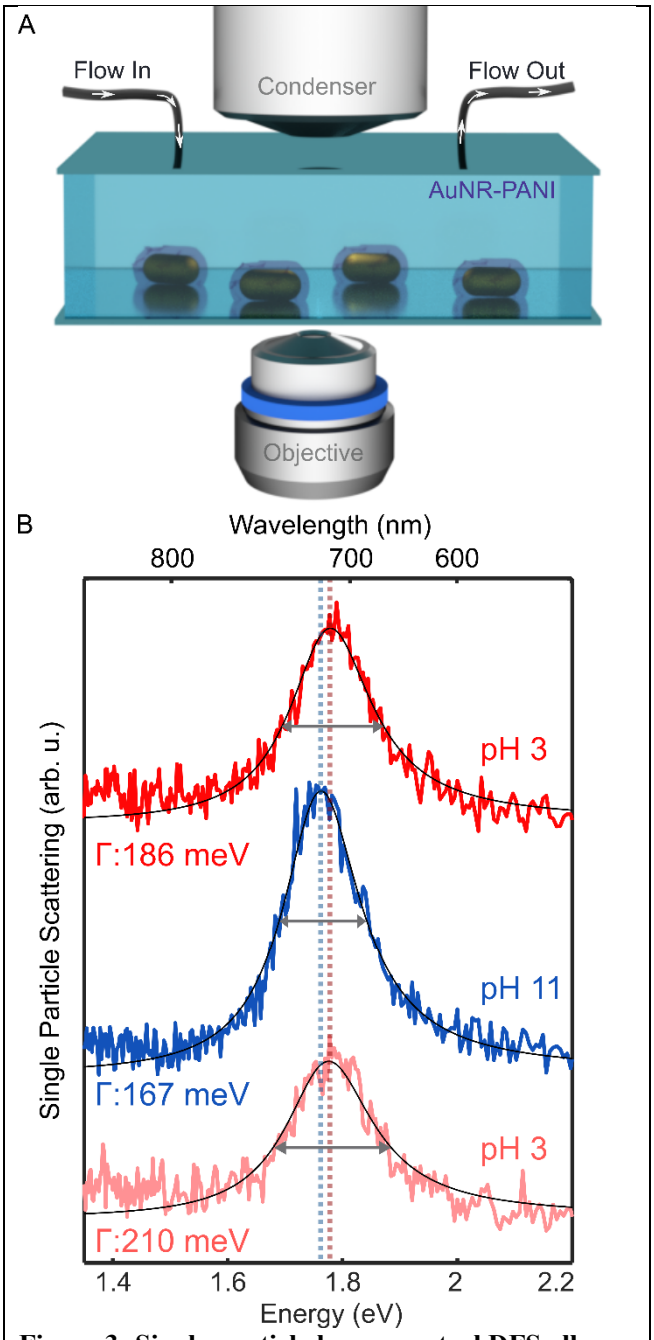

Figure 3: Single-particle hyperspectral DFS allows reversible *in situ* monitoring of AuNR-PANI hybrids in a fluidic cell. A) Schematic of the microfluidic cell atop an inverted hyperspectral dark-field microscope. B) Single-particle spectra of a AuNR-PANI hybrid as the environment is switched from pH 3 (red, E_{res}: 1.77 eV) to pH 11 (blue, E_{res}: 1.74 eV) and back to pH 3 (light red, E_{res}: 1.76 eV) conditions. Single-particle spectra are offset to show changes to E_{res} and Γ.

during the pH transitions, Figure 3B demonstrates the pH dependent dynamic damping. In acidic conditions, the intensity decreases while the Γ and E_{res} increase.

A statistical comparison of spectra from many single-AuNR-PANI hybrids confirms that the plasmon increases in E_{res} and damped in acidic pH conditions, as shown in Figure 4. The E_{res} of 165 single-particles increases as the pH is changed from a basic to an acidic environment, as shown by complementary cumulative distribution

functions in Figure 4A. The E_{res} increases as the PANI is protonated. The increase in E_{res}, 0.04 eV, is similar to changes previously reported for nanoparticles with thin PANI shells.[62, 65] The mechanism responsible for this shift is a change in the refractive index associated with the protonation of PANI.

A similar comparison of Γ_{Total} in Figure 4B shows that as the pH is switched from 11 to 3, Γ_{Total} increases by an average of 34 ± 15 meV, which cannot be explained by a refractive index change. One contributor to the observed Γ_{Total} increase is that as the E_{res} of the AuNR-PANI hybrid shifts at lower pH to overlap more with Au interband transitions, Γ_{Bulk} increases. This contribution is calculated in Figure S3A and B and basically has no effect, as the Γ_{Total} still increases on average by 34 ± 15 meV at pH 3. This large increase confirms an additional damping mechanism is present in acidic conditions. Note that Γ_{Rad} and Γ_{Surf} are determined by particle size, which remains the same for each single-AuNR-PANI hybrid while the pH is tuned, and therefore do not affect the change in measured Γ_{Total}.

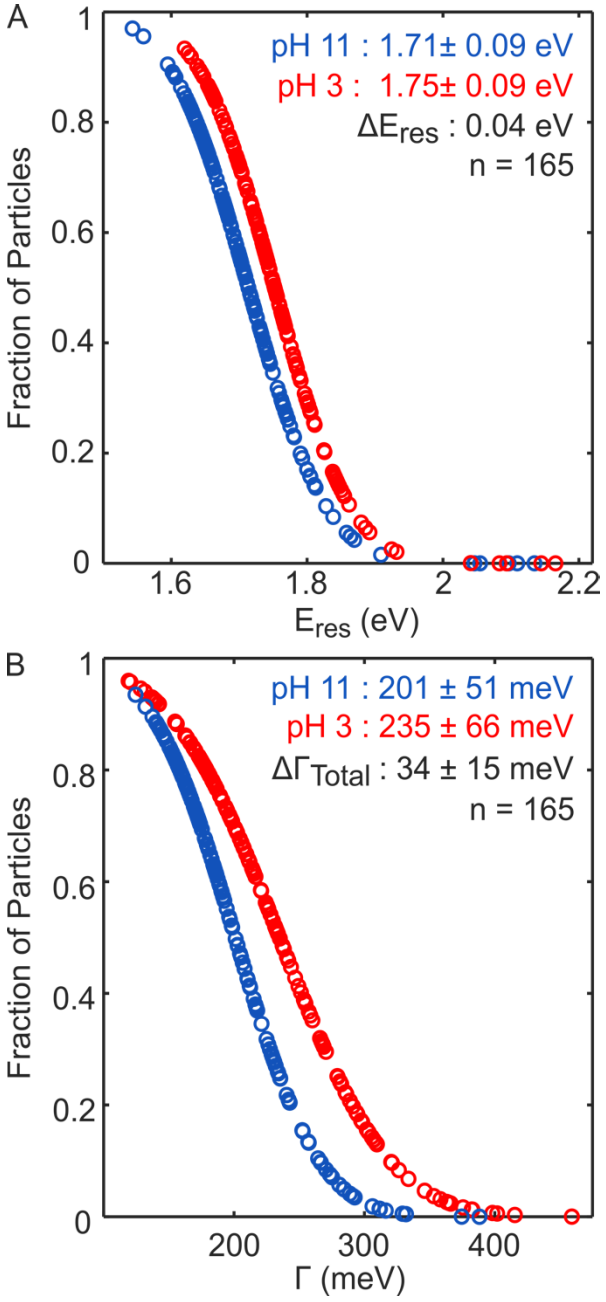

Figure 4: Single-particle statistics confirm that the plasmon of AuNR-PANI hybrids is damped in acidic pH conditions. A) Complimentary cumulative distribution functions of AuNR-PANI hybrid E_{res} show an increase from pH 11 (blue) to pH 3 (red) conditions, 1.71 ± 0.09 to 1.75 ± 0.09 eV, respectively, n=165. B) Complimentary cumulative distribution functions of single-particle Γ_{Total} show an increase from pH 11 (blue) to pH 3 (red) conditions, 201 ± 51 to 235 ± 66 meV, respectively, n=165.

A correlated comparison of the changes in the E_{res} and Γ from individual AuNR-PANI hybrids at pH 11 and pH 3 supports that refractive index changes can account entirely for the shifts in E_{res}, while an additional, and at first glance, more complex, mechanism is required to explain the Γ broadening (Figure 5). Figure 5A shows the E_{res} for correlated AuNR-PANI hybrids in acidic and basic pH conditions. Previous work established PANI's refractive index decreases when protonated, and the decrease in refractive index leads to an increase in the AuNR E_{res}.[59, 66] The experimental ΔE_{res}, 39 meV, is similar in magnitude to ΔE_{res} in previously investigated plasmonic-PANI hybrids.[67] The PANI shell does not completely fill the AuNR sensing volume, 6.6 nm on average for the AuNR-PANI hybrid.[68] The average PANI thickness as calculated from TEM for the tips and sides is 3.4 and 5.7 nm, respectively, shown in Figure S4. The green point in Figure 5A illustrates the change in E_{res} from finite-difference time-domain (FDTD) simulations given in Figure S4. The simulated ΔE_{res}, 67 meV, is slightly larger than the experimental ΔE_{res}. One likely explanation for the difference between the calculated and measured values is that water penetration into the PANI shell also contributes to the effective refractive index sensed by the AuNR.[69]

Figure 5B compares the correlated Γ for 165 AuNRs, which exhibit a more complicated relationship than seen for E_{res}. The Γ in Figure 5B are plotted after removing contributions from Γ_{Bulk}, $\Gamma_{Rad,}$ and Γ_{Surf}, leaving only $\Gamma_{CID.}$ Γ_{Bulk} is removed using the E_{res} dependent Au bulk damping, shown in Figure S3A. Γ_{Rad} of 2.3 meV is subtracted based on the average AuNR volume. Γ_{Surf} is calculated to be 15 meV, assuming an A parameter of 0.12 determined for bare AuNRs as further explained in Figure S1.[30, 63] Unlike for E_{res}, the Γ increases at pH 3 for 81% of the AuNR-PANI hybrids, but not for all. For a portion of single AuNR-PANI hybrids the Γ increases by 50% when the pH is changed from 3 to 11, and for other hybrids there is no change in Γ, despite consistent active switching for E_{res} for the same hybrids under the same conditions. This data, and the inconsistent trends, suggest an additional, nonlinear mechanism for the increased damping.

Accounting for the E_{res} dependent changes in the Γ for all of the AuNR-PANI hybrids can explain the apparent inconsistencies in the data shown in Figures 5A,B, and allow us to assign a mechanism of

RET, as opposed to CT, for CID, as shown in Figures 5C,D. CID encompasses multiple mechanisms, including adsorbate-induced dipole scattering, CT, and RET, all of which lead to accelerated decay of the plasmon.[64] CID can contribute to a large percentage of the total plasmon damping, and which of these is the dominant mechanism can be determined based on the hybrid electronic structure and the chemical nature of the interface.[64] Damping due to dipole scattering occurs when the chemical adsorbate has a static molecular dipole moment that creates an image dipole inside the metal, a resonance independent phenomenon. CT is an interfacial decay pathway, not depending on the acceptor thickness, yet must meet band alignment energy requirements between the donor and acceptor.[37] The addition of the PANI induces plasmon damping due to CID, possibly a result of interfacial CT. CT has been shown to be independent of E_{res}, however, and here we see an E_{res} dependence on the extent of plasmon damping.[17, 70] However, the change in the Γ seen as the pH tunes the spectral overlap between the AuNR and the PANI, as shown in Figure 5B, points to RET. RET, unlike adsorbate-induced dipole scattering, occurs when the plasmon oscillation couples with the polymer transition dipole moment.

Size heterogeneity within the AuNR sample provides an internal control for RET, because corresponding shifts in E_{res} as a function of rod length determine whether the strongest spectral overlap between the E_{res} of the AuNR and PANI's absorption occurs in acidic or basic conditions (Figure 5C). The spectral overlap determines the dipole-dipole coupling strength between the donor (in this case, AuNR) and acceptor (in this case, PANI), and thus the effective η_{RET}. In even the most homogeneous AuNR sample, there is a range of AuNR aspect ratios, causing different E_{res} values, which contributes to heterogeneous broadening in ensemble measurements. But for single-particle DFS, this range in E_{res} provides a set of un-broadened scattering spectra that have varying spectral overlaps with the two forms of PANI. Intrinsic sample heterogeneity therefore acts as an internal spectrometer for our analysis.

Lorentzian fits to the scattering spectra of two representative AuNRs with different E_{res} (black), and the extinction spectra of PANI in acidic (red) and basic (blue) conditions are shown in Figure 5C. The areas where each AuNR spectrally overlaps with the acidic PANI spectrum are shaded red, while regions

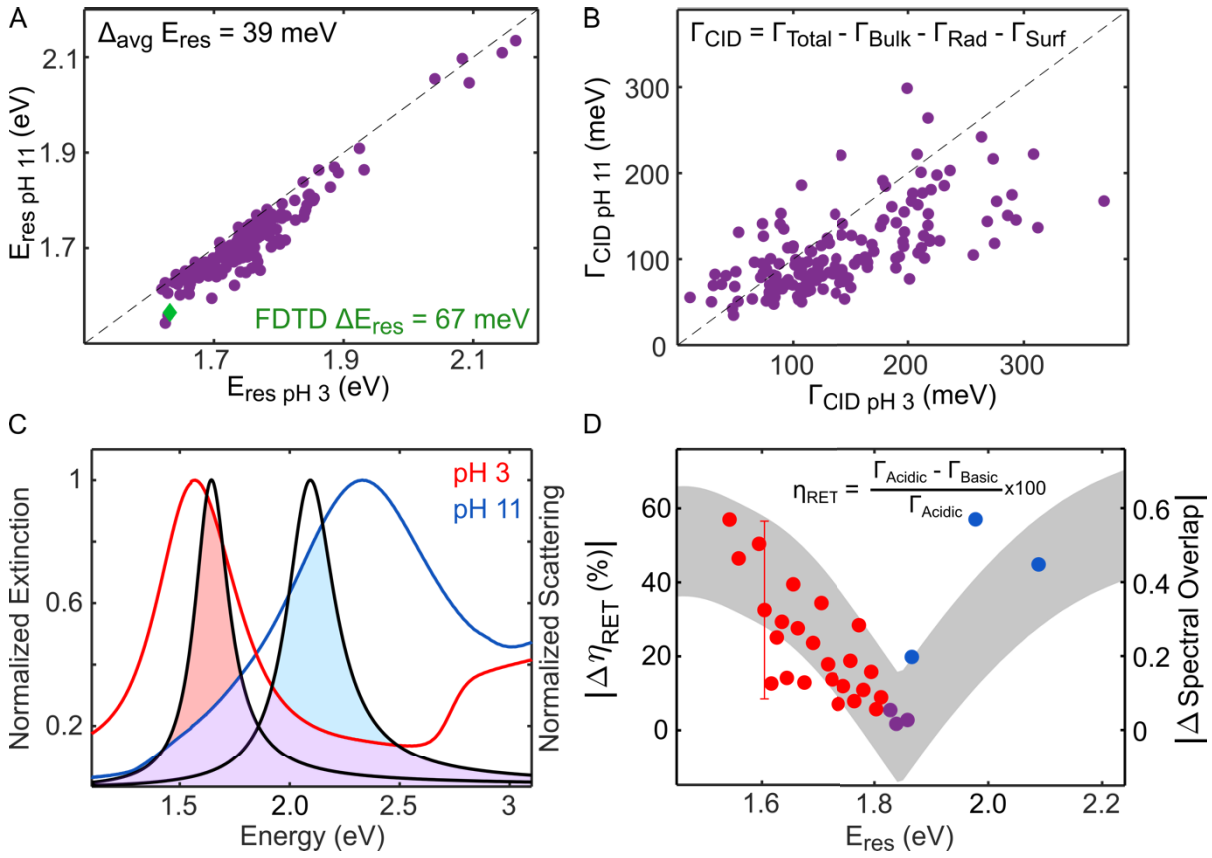

Figure 5: Efficient RET is achieved when spectral overlap is greatest. A) Correlation plot of E_{res} for individual AuNR-PANI hybrids at pH 3 and pH 11. Green data point: FDTD simulated ΔE_{res} for a AuNR-PANI hybrid, see Figure S4. B) Correlation plot of Γ_{CID} for individual AuNR-PANI hybrids at pH 3 and pH 11. Γ_{Bulk}, $\Gamma_{Rad,}$ and Γ_{Surf} contributions to damping have been removed. The dotted lines in A and B represent a 1:1 line of the data presented. C) Spectral overlap of two AuNR-PANI hybrid Lorentzian fits for different AuNR lengths (black), having different E_{res} of 1.65 eV and 2.10 eV. Extinction spectra for acidic (red) and basic (blue) PANI supernatant solutions are shown for comparison. The red and blue shaded regions represent where spectral overlap occurs in acidic and basic conditions, respectively. The purple shaded region represents no change in spectral overlap in both pH conditions. D) The relative change, $\Delta\eta_{RET}$, at acidic and basic conditions vs the E_{res} of the AuNR-PANI hybrids at pH 11. The data points are binned in 0.10 eV intervals. Inset shows how the $\Delta\eta_{RET}$ is calculated from differences in measured Γ. The data points are colored to match the regions where the change in spectral overlap occurs, illustrated in panel C. The red data points represent where spectral overlap is greatest at pH 3, blue where it is greatest at pH 11, and purple where the values are unchanged. The gray shaded region shows the standard deviation of the calculated absolute change in spectral overlap at pH 3 vs pH 11. Spectral overlap was calculated at both pH 3 and 11 for a Lorentzian shifted across the energy scale by calculating the area under the curve, as illustrated in Figure S5. The $\Delta\eta_{RET}$ follows the spectral overlap showing the tunability of RET based on particle E_{res} and the PANI protonation state.

that overlap with the basic PANI spectrum are shaded blue. The purple-shaded region in Figure 5C

denotes the regions where there is no change expected in the spectral overlap when the pH is switched.

More details for the calculation of this region are included in Figure S5, but briefly, due to the broad absorption of PANI, AuNRs with E_{res} near 1.8 eV have equal amounts of spectral overlap at both pH conditions. Shorter AuNR-PANI hybrids with E_{res} higher than 1.8 eV have greater spectral overlap at pH 11 and thus increased RET, observed as increased Γ_{CID} at basic conditions. In contrast, longer AuNR-PANI hybrids with E_{res} lower than 1.8 eV have better spectral overlap at pH 3, resulting in increased RET at acidic conditions. This switch between optimal conditions for RET as a function of AuNR size and pH implies that there should be an inversion point in η_{RET} around 1.8 eV.

Calculated $\Delta\eta_{RET}$, shown in Figure 5D for AuNR-hybrids with various E_{res} values, confirms an inversion point around 1.8 eV and strongly supports that RET is responsible for the experimentally observed increase in the Γ at pH 3. To determine if the change in the Γ is E_{res} dependent, the absolute percent change in the RET contribution to the Γ when switching from acidic to basic conditions is plotted. The E_{res} dependent $\Delta\eta_{RET}$ is given as the relative change in the Γ between pH conditions, shown in Figure 5D. Only η_{RET} defined as $\Gamma_{CID=RET} / \Gamma_{Total}$ (Figures S3B and S3C) is not sufficient to resolve the E_{res} dependence as shown in Figure S3D. The $\Delta\eta_{RET}$ data is binned every 0.10 eV to clearly present the RET E_{res} dependence of 165 AuNRs. The red data points represent the AuNRs where the spectral overlap is greatest with the acidic conditions, corresponding to Figure 5C. The blue data points represent those with more spectral overlap in basic conditions, while the purple points represent those AuNRs with no change in the spectral overlap integral as the pH is switched. To visualize the spectral overlap integral between the AuNR and the PANI, the absolute value of the spectral overlap integral is plotted. The gray-shaded region in Figure 5D represents one standard deviation of the spectral overlap integral, calculated by integrating the area under a Lorentzian fit to a representative AuNR and the PANI absorption in both pH conditions, further detailed in Figure S5 and visualized in Figure 5C. The overlaid absolute change in spectral overlap matches well with the experimental data, identifying that $\Delta\eta_{RET}$ has a strong E_{res} dependence as a result of the change in the spectral overlap integral. The data clearly exhibits an inversion point, with η_{RET} increasing where the difference in spectral overlap is the greatest, at energies both below and above 1.8 eV for acidic and basic conditions, respectively. Due to the initial E_{res} of the AuNR sample,

1.73 eV, used for PANI hybridization there are fewer AuNR-PANI hybrids at E_{res} > 1.8 eV, highlighting the importance of single-particle measurements to uncover this E_{res} dependent change in $\Delta\eta_{RET}$.

In conclusion, we identified RET as a new type of interaction between AuNR donors and PANI acceptors under reversible protonation of the PANI shell, only possible due to single-particle resolution. The E_{res} dependent η_{RET} reported in this system highlights a previously unreported plasmon damping mechanism in AuNR-PANI hybrids. The dynamic tunability of η_{RET} by varying the PANI absorption through changes of the solution pH allows the AuNR-PANI hybrid RET to be turned on and off *in situ*. For our system, shorter AuNRs with higher E_{res} have greater spectral overlap in basic conditions, whereas longer AuNRs with lower E_{res} have greater spectral overlap in acidic conditions. Single-particle measurements made it possible to map out the spectral dependence of $\Delta\eta_{RET}$ when changing the pH because of variation in the E_{res} of the AuNRs using the same hybrid sample. Although the change in the Γ is much larger between the bare and PANI coated AuNRs (Figure 2) compared to when the pH is tuned (Figure 4), *in situ* Γ tuning and the dispersity in aspect ratio and hence E_{res} made it possible to clearly assign CID to RET in AuNR-PANI hybrids. In contrast, the inability to perform correlated DFS of the same AuNRs before and after coating together with electron microscopy hindered the accurate subtraction of the size dependent damping contributions $\Gamma_{Rad,}$ and Γ_{Surf} and therefore a clear assignment of RET. Overall, our findings can be used to capture the energy offered by the plasmon to drive RET-based chemistry efficiently.

Experimental Methods

Materials:

pH solutions: Sodium hydroxide (1N, Thermo Fisher Chemical) was diluted to 1.63 mM, and nitric acid (70%, Sigma-Aldrich) was diluted to 0.25 mM using Milli-Q water. *Synthesis:* Ascorbic acid (AA, >99%), aniline (≥99.5%), hydrogen tetrachloroaurate ($HAuCl_4$, >99.9%), sodium borohydride ($NaBH_4$, 99%), sodium dodecyl sulfate (SDS, ≥99.0%) and silver nitrate ($AgNO_3$, 99.9999%) were

purchased from Sigma-Aldrich. Hexadecyltrimethylammonium bromide (CTAB, 99%) was received from Merck KGaA. Hexadecyltrimethylammonium chloride (CTAC, >99%) was obtained from Molekula. Ammonium peroxosulfate (APS, ≥98%) was obtained from Honeywell. Hydrochloric acid (HCl, AnalaR Normapur, 37%) was purchased from VWR Chemicals. Sodium hydroxide (NaOH, 1N solution) was obtained from J.T. Baker. All chemicals and solvents were used as received. Purified water (Milli-Q grade, 18.2 MΩ cm at 25 °C) was used throughout the whole synthesis.

AuNR-PANI Hybrid Synthesis and Characterization:

Synthesis of AuNRs: AuNRs, shown in Figure S6, of 41 nm length and 14 nm width were synthesized with minor modifications as published elsewhere.[71] Briefly, seed particles were synthesized by adding 300 µL of a freshly prepared 0.01 M $NaBH_4$ solution in a 4.7-mL-mixture of 0.1 M CTAB and 0.25 mM $HAuCl_4$ under vigorous stirring. The solution was stirred rapidly for 2 min followed by continued slow stirring at 32 °C for 30 min. 1 L of a 0.1 M CTAB solution containing 0.25 mM $HAuCl_4$, 0.06 mM $AgNO_3$, 500 µL of a 0.1 M HBr solution to adjust the pH, and 0.35 mM ascorbic acid as reducing agent was prepared. 4 mL of the seeds was then added to this solution after 30 min and mixed thoroughly.

Synthesis of the PANI Shell: 876 µL aqueous SDS solution (80 mM) and 60 µL HCl (1 M) were added to 8.2 mL water. Under vigorous stirring, 2 mL of AuNR suspension (2 mM Au0, 1 mM CTAC) was added. Subsequently, 1.2 mL of aqueous aniline solution (10 mM) was added. The polymerization was initiated by adding 1.5 mL of aqueous APS solution (13.33 mM). After one hour, the stirring speed was reduced, and the reaction mixture was stirred for another 4 hours. The PANI-coated AuNRs were purified by three centrifugation-re-dispersion cycles (8500 rcf for 30 min, re-dispersion in 5 mM SDS solution). The supernatant from the first centrifugation cycle was kept for UV-vis-NIR measurements.

UV-vis-NIR Spectroscopy: Extinction spectra were acquired with a Cary 5000 spectrophotometer (Agilent Technologies Deutschland GmbH). The value of the extinction spectrum at a wavelength of 400

nm (interband transitions of Au) was used to calculate the concentration of the AuNR dispersions.[72] For the pH-dependent extinction measurements, aqueous solutions of 5 mM SDS were adjusted to pH 3 and pH 11 by adding 1 M HCl and 1 M NaOH, respectively.

Single-AuNR Sample Preparation: 600 µL (12 x 50 µL) of bare AuNRs or AuNR-PANI hybrids were spun cast onto glass slides at 3000 rpm for 60 seconds for each cycle. Bare AuNRs (14 x 41 nm) and AuNR-PANI hybrids were deposited to achieve an approximate particle density of $\sim 5 \times 10^{-5}$ AuNRs/mm^2. Glass slides were oxygen plasma cleaned for 2 min directly before spin casting.

Fluidic Cell Preparation: Adhesive 0.8 mm thick silicon spacers (Grace Bio-Laboratories) were cut to create a microfluidic channel for incorporation onto the microscope. The fluidic cell was then assembled by sandwiching two 50 x 75 mm, 0.17 mm thick glass coverslips (Brain Research Lab) together using the adhesive silicon spacer with the top glass having two 1 mm diameter openings laser cut at the corners to create the flow channel. The cell was placed in a custom-made sample holder and pressured sealed. Tubing and a syringe were used to create a vacuum in the fluidic chamber allowing the solution in the cell to be changed while on the microscope.

In Situ Hyperspectral Imaging: Dark-field scattering (DFS) spectra of individual bare AuNRs and AuNR-PANI hybrids were measured using a hyperspectral dark-field microscope.[73] A Zeiss AxioObserver m1 inverted dark-field microscope body was fitted with an oil immersion condenser (numerical aperture NA=1.4) focusing light from a 100 W tungsten-halogen lamp (at 3200 K) to the sample plane. Scattering from the AuNRs and AuNR-PANI hybrids was collected using an oil immersion objective (Zeiss, PlanAchromat 63x, NA=0.7). Collected light moved through a mechanical slit (20 µm) into a spectrograph (Princeton Instruments, Acton SP2150i) with a diffraction grating (800 nm blaze wavelength, 150 lines/mm). The spectrally dispersed light was then sent to a camera (Princeton Instruments, PIXIS 400). The spectrograph and camera setup were mounted on a translation stage, allowing the accumulation of a hyperspectral data cube. Data acquisition and instrument control were

achieved using NI LabVIEW software with customized sub-routines. Hyperspectral images were taken with an integration time of 5 seconds per pixel. Hyperspectral images were acquired for high and low pH conditions using sodium hydroxide and nitric acid solutions. To ensure full protonation occurred using nitric acid, a control experiment was performed with HCl, and the same spectral changes were observed (Figure S7). All AuNR and AuNR-PANI hybrid DFS spectra were fit to a single Lorentzian function using a nonlinear least squares fitting routine implemented in MATLAB 2016b. Particles were correlated across pH conditions to observe changes in E_{res} and Γ.

ASSOCIATED CONTENT

Supporting Information ~~available:~~

- Characterization of AuNR sample
- Additional supporting single particle data showing reversible changes in RET
- Additional supporting single particle data during protonation with HCL
- Calculations of CID, RET, and spectral overlap analysis of AuNR-PANI hybrids
- Simulations of the of the AuNR-PANI hybrid ΔE_{res} between different pH conditions

AUTHOR INFORMATION

Corresponding Authors

Stephan Link - *Department of Chemistry, Department of Electrical and Computer Engineering, Smalley-Curl Institute, Rice University, 6100 Main Street, Houston, Texas 77005, United States,* http://orcid.org/0000-0002-4781-930X; Email: slink@rice.edu

Christy F. Landes - *Department of Chemistry, Department of Electrical and Computer Engineering, Smalley-Curl Institute, Department of Chemical and Biomolecular Engineering, Rice University, 6100 Main Street, Houston, Texas 77005, United States,* http://orcid.org/0000-

0003-4163-6497; Email: cflandes@rice.edu

Authors

Annette Jones - *Department of Chemistry, Rice University, 6100 Main Street, Houston, Texas 77005, United States*, https://orcid.org/0000-0001-5342-0947

Emily K. Searles - *Department of Chemistry, Rice University, 6100 Main Street, Houston, Texas 77005, United States*, https://orcid.org/0000-0001-8621-0110

Martin Mayer - *Leibniz-Institut für Polymerforschung Dresden e.V., Institute of Physical Chemistry and Polymer Physics, Dresden, Germany,* https://orcid.org/0000-0003-4013-1892

Marisa Hoffmann - *Leibniz-Institut für Polymerforschung Dresden e.V., Institute of Physical Chemistry and Polymer Physics, Dresden, Germany,* https://orcid.org/0000-0001-6604-7782

Niklas Gross - *Department of Chemistry, Rice University, 6100 Main Street, Houston, Texas 77005, United States,* https://orcid.org/0000-0002-2425-1029

Hyuncheol Oh - *Department of Chemistry, Rice University, 6100 Main Street, Houston, Texas 77005, United States*

Andreas Fery - *Leibniz-Institut für Polymerforschung Dresden e.V., Institute of Physical Chemistry and Polymer Physics, Dresden, Germany,* https://orcid.org/0000-0001-6692-3762

Notes

The authors declare no competing financial interests.

ACKNOWLEDGMENTS

Funding: This work was primarily supported by the National Science Foundation, Center for Adopting Flaws as Features (NSF CHE 2124983). CFL acknowledges the Kenneth S. Pitzer-Schlumberger Chari in Chemistry. SL thanks the Robert A. Welch Foundation for support through the Charles W. Duncan, Jr.-

Welch Chair in Chemistry (C-0002). The Fery group gratefully acknowledges the financial support from the Deutsche Forschungsgemeinschaft (DFG) within RTG2767, project no. 451785257. The studies were performed within the LaSensA project carried out under the M-ERA.NET 2 scheme (European Union's Horizon 2020 research and innovation program, grant No. 685451) and co-funded by the Research Council of Lithuania (LMTLT), agreement No. S-M-ERA.NET-21-2, the National Science Centre of Poland, project No. 2020/02/Y/ST5/00086, and the Saxon State Ministry for Science, Culture and Tourism (Germany), grant No. 100577922, as well as from the tax funds on the basis of the budget passed by the Saxon state parliament. M.M. gratefully acknowledges funding by the Deutsche Forschungsgemeinschaft (DFG, German Research Foundation, 453211202.)

References:

1. Atwater, H. A.; Polman, A., Plasmonics for Improved Photovoltaic Devices. *Nat. Mater.* **2010,** *9*, 205-213.
2. Brongersma, M. L.; Halas, N. J.; Nordlander, P., Plasmon-Induced Hot Carrier Science and Technology. *Nat. Nanotechnol.* **2015,** *10*, 25-34.
3. Schuller, J. A.; Barnard, E. S.; Cai, W.; Jun, Y. C.; White, J. S.; Brongersma, M. L., Plasmonics for Extreme Light Concentration and Manipulation. *Nat. Mater.* **2010,** *9*, 193-204.
4. Mayer, K. M.; Hafner, J. H., Localized Surface Plasmon Resonance Sensors. *Chem. Rev.* **2011,** *111*, 3828-3857.
5. Hu, M.; Chen, J.; Li, Z. Y.; Au, L.; Hartland, G. V.; Li, X.; Marquez, M.; Xia, Y., Gold Nanostructures: Engineering their Plasmonic Properties for Biomedical Applications. *Chem. Soc. Rev.* **2006,** *35*, 1084.
6. Lal, S.; Link, S.; Halas, N. J., Nano-optics from Sensing to Waveguiding. *Nat. Photon* **2007,** *1*, 641-648.
7. Kelly, K. L.; Coronado, E.; Zhao, L. L.; Schatz, G. C., The Optical Properties of Metal Nanoparticles: The Influence of Size, Shape, and Dielectric Environment. *J. Phys. Chem. B* **2003,** *107*, 668-677.
8. Becker, J.; Schubert, O.; Sönnichsen, C., Gold Nanoparticle Growth Monitored in situ Using a Novel Fast Optical Single-Particle Spectroscopy Method. *Nano Lett.* **2007,** *7* 1664-1669.
9. Cheng, J.; Liu, Y.; Cheng, X.; He, Y.; Yeung, E. S., Real Time Observation of Chemical Reactions of Individual Metal Nanoparticles with High-Throughput Single Molecule Spectral Microscopy. *Anal. Chem.* **2010,** *82*, 8744-8749.
10. Tebbe, M.; Kuttner, C.; Mayer, M.; Maennel, M.; Pazos-Perez, N.; König, T. A. F.; Fery, A., Silver-Overgrowth-Induced Changes in Intrinsic Optical Properties of Gold Nanorods: From Noninvasive Monitoring of Growth Kinetics to Tailoring Internal Mirror Charges. *J. Phys. Chem. C* **2015,** *119*, 9513-9523.
11. Jiang, D.; Chen, H. B.; Zhou, X. L.; Liu, X. W., Single-Particle Electrochemical Imaging Provides Insights into Silver Nanoparticle Dissolution at the Solution–Solid Interface. *ACS Appl. Mater. Interfaces* **2022,** *14*, 22658-22665.
12. Al-Zubeidi, A.; Stein, F.; Flatebo, C.; Rehbock, C.; Hosseini Jebeli, S. A.; Landes, C. F.; Barcikowski, S.; Link, S., Single-Particle Hyperspectral Imaging Reveals Kinetics of Silver Ion Leaching from Alloy Nanoparticles. *ACS Nano* **2021,** *15*, 8363-8375.
13. Flatebo, C.; Collins, S. S. E.; Hoener, B. S.; Cai, Y. Y.; Link, S.; Landes, C. F., Electrodissolution Inhibition of Gold Nanorods with Oxoanions. *J. Phys. Chem. C* **2019,** *123*, 13983-13992.
14. Mock, J. J.; Smith, D. R.; Schultz, S., Local Refractive Index Dependence of Plasmon Resonance Spectra from Individual Nanoparticles. *Nano Lett.* **2003,** *3*, 485-491.
15. Chen, H.; Kou, X.; Yang, Z.; Ni, W.; Wang, J., Shape- and Size-Dependent Refractive Index Sensitivity of Gold Nanoparticles. *Langmuir* **2008,** *24*, 5233-5237.
16. Zhan, Y.; Lei, D. Y.; Li, X.; Maier, S. A., Plasmonic Fano Resonances in Nanohole Quadrumers for Ultra-Sensitive Refractive Index Sensing. *Nanoscale* **2014,** *6*, 4705-4715.
17. Wu, K.; Chen, J.; McBride, J. R.; Lian, T., Efficient Hot-Electron Transfer by a Plasmon-Induced Interfacial Charge-Transfer Transition. *Science* **2015,** *349*, 632-635.
18. Anderson, N. A.; Lian, T., Ultrafast Electron Transfer at the Molecule-Semiconductor Nanoparticle Interface. *Annu. Rev. Phys. Chem.* **2005,** *56*, 491-519.
19. Liu, Y.; Chen, Q.; Cullen, D. A.; Xie, Z.; Lian, T., Efficient Hot Electron Transfer from Small Au Nanoparticles. *Nano Lett.* **2020,** *20*, 4322-4329.
20. Lim, S. C.; Lo, W. F.; Yang, P. Y.; Lu, S. C.; Joplin, A.; Link, S.; Chang, W. S.; Tuan, H.-Y., Au@CdSe Heteroepitaxial Nanorods: An Example of Metal Nanorods Fully Covered by a Semiconductor Shell with Strong Photo-Induced Interfacial Charge Transfer Effects. *J. Colloid Interface Sci.* **2018,** *532*, 143-152.

21. Hsu, L.-Y.; Ding, W.; Schatz, G. C., Plasmon-Coupled Resonance Energy Transfer. *J. Phys. Chem. Lett.* **2017,** *8*, 2357-2367.
22. Cushing, S. K.; Li, J.; Meng, F.; Senty, T. R.; Suri, S.; Zhi, M.; Li, M.; Bristow, A. D.; Wu, N., Photocatalytic Activity Enhanced by Plasmonic Resonant Energy Transfer from Metal to Semiconductor. *J. Am. Chem. Soc.* **2012,** *134*, 15033-15041.
23. Cushing, S. K.; Li, J.; Bright, J.; Yost, B. T.; Zheng, P.; Bristow, A. D.; Wu, N., Controlling Plasmon-Induced Resonance Energy Transfer and Hot Electron Injection Processes in Metal@TiO2 Core–Shell Nanoparticles. *J. Phys. Chem. C* **2015,** *119*, 16239-16244.
24. Collins, S. S. E.; Searles, E. K.; Tauzin, L. J.; Lou, M.; Bursi, L.; Liu, Y.; Song, J.; Flatebo, C.; Baiyasi, R.; Cai, Y. Y.; Foerster, B.; Lian, T.; Nordlander, P.; Link, S.; Landes, C. F., Plasmon Energy Transfer in Hybrid Nanoantennas. *ACS Nano* **2020**, 9522-9530.
25. Vyas, V. S.; Lau, V. W. H.; Lotsch, B. V., Soft Photocatalysis: Organic Polymers for Solar Fuel Production. *Chem. Mater.* **2016,** *28*, 5191-5204.
26. Linic, S.; Aslam, U.; Boerigter, C.; Morabito, M., Photochemical Transformations on Plasmonic Meal Nanoparticles. *Nat. Mater.* **2015,** *14*, 567.
27. Li, J.; Cushing, S. K.; Bright, J.; Meng, F.; Senty, T. R.; Zheng, P.; Bristow, A. D.; Wu, N., Ag@Cu2O Core-Shell Nanoparticles as Visible-Light Plasmonic Photocatalysts. *ACS Catal.* **2013,** *3*, 47-51.
28. Ferry, V. E.; Sweatlock, L. A.; Pacifici, D.; Atwater, H. A., Plasmonic Nanostructure Design for Efficient Light Coupling into Solar Cells. *Nano Lett.* **2008,** *8*, 4391-4397.
29. Hoffmann, M.; Schletz, D.; Steiner, A. M.; Wolf, D.; Mayer, M.; Fery, A., Conjugated Polymer–Gold–Silver Hybrid Nanoparticles for Plasmonic Energy Focusing. *J. Phys. Chem. C* **2022,** *126*, 2475-2481.
30. Foerster, B.; Joplin, A.; Kaefer, K.; Celiksoy, S.; Link, S.; Sönnichsen, C., Chemical Interface Damping Depends on Electrons Reaching the Surface. *ACS Nano* **2017,** *11*, 2886-2893.
31. Foerster, B.; Spata, V. A.; Carter, E. A.; Sönnichsen, C.; Link, S., Plasmon Damping Depends on the Chemical Nature of the Nanoparticle Interface. *Sci. Adv.* **2019,** *5*, eaav0704.
32. Hoggard, A.; Wang, L. Y.; Ma, L.; Fang, Y.; You, G.; Olson, J.; Liu, Z.; Chang, W. S.; Ajayan, P. M.; Link, S., Using the Plasmon Linewidth To Calculate the Time and Efficiency of Electron Transfer between Gold Nanorods and Graphene. *ACS Nano* **2013,** *7*, 11209-11217.
33. Celiksoy, S.; Ye, W.; Wandner, K.; Kaefer, K.; Sönnichsen, C., Intensity-Based Single Particle Plasmon Sensing. *Nano Lett.* **2021,** *21*, 2053-2058.
34. Liu, G.; Lou, Y.; Zhao, Y.; Burda, C., Directional Damping of Plasmons at Metal–Semiconductor Interfaces. *Acc. Chem. Res.* **2022,** *55*, 1845-1856.
35. Devasia, D.; Das, A.; Mohan, V.; Jain, P. K., Control of Chemical Reaction Pathways by Light–Matter Coupling. *Annu. Rev. Phys. Chem.* **2021,** *72*, 423-443.
36. Kale, M. J.; Christopher, P., Plasmons at the Interface. *Science* **2015,** *349* (6248), 587-588.
37. Lee, S. A.; Ostovar, B.; Landes, C. F.; Link, S., Spectroscopic Signatures of Plasmon-Induced Charge Transfer in Gold Nanorods. *J. Chem. Phys.* **2022,** *156*, 064702.
38. Luna, M.; Barawi, M.; Gómez-Moñivas, S.; Colchero, J.; Rodríguez-Peña, M.; Yang, S.; Zhao, X.; Lu, Y.-H.; Chintala, R.; Reñones, P., Photoinduced Charge Transfer and Trapping on Single Gold Metal Nanoparticles on TiO2. *ACS Appl. Mater. Interfaces* **2021,** *13*, 50531-50538.
39. Ahlawat, M.; Mittal, D.; Govind Rao, V., Plasmon-induced Hot-Hole Generation and Extraction at Nano-Heterointerfaces for Photocatalysis. *Comm. Mater.* **2021,** *2*, 1-15.
40. Li, J.; Cushing, S. K.; Meng, F.; Senty, T. R.; Bristow, A. D.; Wu, N., Plasmon-induced Resonance Energy Transfer for Solar Energy Conversion. *Nat. Photon* **2015,** *9*, 601-607.
41. Steiner, A. M.; Lissel, F.; Fery, A.; Lauth, J.; Scheele, M., Prospects of Coupled Organic–Inorganic Nanostructures for Charge and Energy Transfer Applications. *Angew. Chem.* **2021,** *60*, 1152-1175.

42. Moroz, P.; Razgoniaeva, N.; Vore, A.; Eckard, H.; Kholmicheva, N.; McDarby, A.; Razgoniaev, A. O.; Ostrowski, A. D.; Khon, D.; Zamkov, M., Plasmon-Induced Energy Transfer: When the Game Is Worth the Candle. *ACS Photonics* **2017,** *4*, 2290-2297.
43. Chen, H.; Shao, L.; Woo, K. C.; Wang, J.; Lin, H. Q., Plasmonic–Molecular Resonance Coupling: Plasmonic Splitting versus Energy Transfer. *J. Phys. Chem. C* **2012,** *116*, 14088-14095.
44. Ma, X. C.; Dai, Y.; Yu, L.; Huang, B. B., Energy Transfer in Plasmonic Photocatalytic Composites. *Light Sci. Appl.* **2016,** *5*, e16017.
45. Linic, S.; Christopher, P.; Ingram, D. B., Plasmonic-Metal Nanostructures for Efficient Conversion of Solar to Chemical Energy. *Nat. Mater.* **2011,** *10*, 911-912.
46. Linic, S.; Chavez, S.; Elias, R., Flow and Extraction of Energy and Charge Carriers in Hybrid Plasmonic Nanostructures. *Nat. Mater.* **2021,** *20*, 916-924.
47. Ramakrishnan, S. B.; Mohammadparast, F.; Dadgar, A. P.; Mou, T.; Le, T.; Wang, B.; Jain, P. K.; Andiappan, M., Photoinduced Electron and Energy Transfer Pathways and Photocatalytic Mechanisms in Hybrid Plasmonic Photocatalysis. *Adv. Opt. Mater.* **2021,** *9*, 2101128.
48. Huang, W.-S.; Humphrey, B. D.; MacDiarmid, A. G., Polyaniline, a Novel Conducting Polymer. Morphology and Chemistry of its Oxidation and Reduction in Aqueous Electrolytes. *J. Chem. Soc., Faraday Trans. 1* **1986,** *82*, 2385-2400.
49. Baker, C. O.; Huang, X.; Nelson, W.; Kaner, R. B., Polyaniline Nanofibers: Broadening Applications for Conducting Polymers. *Chem. Soc. Rev.* **2017,** *46*, 1510-1525.
50. Beygisangchin, M.; Abdul Rashid, S.; Shafie, S.; Sadrolhosseini, A. R.; Lim, H. N., Preparations, Properties, and Applications of Polyaniline and Polyaniline Thin Films—A Review. *Polymers* **2021,** *13*, 2003.
51. Hu, M.; Novo, C.; Funston, A.; Wang, H.; Staleva, H.; Zou, S.; Mulvaney, P.; Xia, Y.; Hartland, G. V., Dark-Field Microscopy Studies of Single Metal Nanoparticles: Understanding the Factors that Influence the Linewidth of the Localized Surface Plasmon Resonance. *J. Mater. Chem.* **2008,** *18*, 1949-1960.
52. Rudayni, F.; Kafle, T. R.; Waters, J.; Rijal, K.; Chan, W. L., Ultrafast and Long-Range Energy Transfer from Plasmon to Molecular Exciton. *J. Phys. Chem. C* **2023,** *127*, 1697-1703.
53. Peng, J.; Lin, Q.; Földes, T.; Jeong, H.-H.; Xiong, Y.; Pitsalidis, C.; Malliaras, G. G.; Rosta, E.; Baumberg, J. J., In-Situ Spectro-Electrochemistry of Conductive Polymers Using Plasmonics to Reveal Doping Mechanisms. *ACS Nano* **2022,** *16*, 21120-21128.
54. Huang, W.; MacDiarmid, A., Optical Properties of Polyaniline. *Polymer* **1993,** *34*, 1833-1845.
55. Lu, W.; Jiang, N.; Wang, J., Active Electrochemical Plasmonic Switching on Polyaniline-Coated Gold Nanocrystals. *Adv. Mater. (Weinheim, Ger.)* **2017,** *29*.
56. Chu, K.-Y.; Griffiths, J., Naphthoquinone Colouring Matters. Part 1. Synthesis and electronic Absorption Spectra of 1, 4-naphthoquinone Derivatives with Electron-Donating Groups in the Quinonoid Ring. *J. Chem. Soc., Perkins trans.* **1978,** 1083-1087.
57. Cromack, K.; Jozefowicz, M.; Ginder, J.; Epstein, A. J.; McCall, R.; Du, G.; Leng, J.; Kim, K.; Li, C., Thermal Process for Orientation of Polyaniline Films. *Macromolecules* **1991,** *24*, 4157-4161.
58. Pensa, E.; Gargiulo, J.; Lauri, A.; Schlücker, S.; Cortés, E.; Maier, S. A., Spectral Screening of the Energy of Hot Holes over a Particle Plasmon Resonance. *Nano Lett.* **2019,** *19*, 1867-1874.
59. Tian, L.; Chen, E.; Gandra, N.; Abbas, A.; Singamaneni, S., Gold Nanorods as Plasmonic Nanotransducers: Distance-Dependent Refractive Index Sensitivity. *Langmuir* **2012,** *28*, 17435-17442.
60. Foerster, B.; Rutten, J.; Pham, H.; Link, S.; Sönnichsen, C., Particle Plasmons as Dipole Antennas: State Representation of Relative Observables. *J. Phys. Chem. C* **2018,** *122*, 19116-19123.
61. Ledin, P. A.; Jeon, J. W.; Geldmeier, J. A.; Ponder, J. F.; Mahmoud, M. A.; El-Sayed, M.; Reynolds, J. R.; Tsukruk, V. V., Design of Hybrid Electrochromic Materials with Large Electrical Modulation of Plasmonic Resonances. *ACS Appl. Mater. Interfaces* **2016,** *8*, 13064-13075.
62. Jeon, J.-W.; Zhou, J.; Geldmeier, J. A.; Ponder, J. F.; Mahmoud, M. A.; El-Sayed, M.; Reynolds, J. R.; Tsukruk, V. V., Dual-Responsive Reversible Plasmonic Behavior of Core–Shell Nanostructures with pH-Sensitive and Electroactive Polymer Shells. *Chem. Mater.* **2016,** *28*, 7551-7563.

63. Novo, C.; Gomez, D.; Perez-Juste, J.; Zhang, Z.; Petrova, H.; Reismann, M.; Mulvaney, P.; Hartland, G. V., Contributions from Radiation Damping and Surface Scattering to the Linewidth of the Longitudinal Plasmon Band of Gold Nanorods: a Single Particle Study. *Phys. Chem. Chem. Phys.* **2006,** *8*, 3540.
64. Lee, S. A.; Link, S., Chemical Interface Damping of Surface Plasmon Resonances. *Acc. Chem. Res.* **2021,** *54*, 1950-1960.
65. Peng, J.; Jeong, H.-H.; Lin, Q.; Cormier, S.; Liang, H.-L.; De Volder, M. F.; Vignolini, S.; Baumberg, J. J., Scalable Electrochromic Nanopixels Using Plasmonics. *Sci. Adv.* **2019,** *5*, eaaw2205.
66. Lu, W.; Cui, X.; Chow, T. H.; Shao, L.; Wang, H.; Chen, H.; Wang, J., Switching Plasmonic Fano Resonance in Gold Nanosphere–Nanoplate Heterodimers. *Nanoscale* **2019,** *11*, 9641-9653.
67. Jiang, N.; Shao, L.; Wang, J., (Gold Nanorod Core)/(Polyaniline Shell) Plasmonic Switches with Large Plasmon Shifts and Modulation Depths. *Adv. Mater.* **2014,** *26*, 3282-3289.
68. Becker, J.; Trügler, A.; Jakab, A.; Hohenester, U.; Sönnichsen, C., The Optimal Aspect Ratio of Gold Nanorods for Plasmonic Bio-Sensing. *Plasmonics* **2010,** *5*, 161-167.
69. Rafiqi, F. A.; Majid, K., Synthesis, Characterization, Photophysical, Thermal and Electrical Properties of Composite of Polyaniline with Zinc Bis (8-hydroxyquinolate): A Potent Composite for Electronic and Optoelectronic Use. *RSC Adv.* **2016,** *6*, 22016-22025.
70. Li, M.; Cushing, S. K.; Wang, Q.; Shi, X.; Hornak, L. A.; Hong, Z.; Wu, N., Size-Dependent Energy Transfer between CdSe/ZnS Quantum Dots and Gold Nanoparticles. *J. Phys. Chem. Lett.* **2011,** *2*, 2125-2129.
71. Tebbe, M.; Cherepanov, P.; Skorb, E.; Poznyak, S. K.; Garcia de Abajo, J.; Fery, A.; Andreeva, D.; Alvarez-Puebla, R.; Pazos-Perez, N., Hierarchical Materials: SERS Platforms of Plasmonic Hydrophobic Surfaces for Analyte Concentration: Hierarchically Assembled Gold Nanorods on Anodized Aluminum. *Part. Part. Syst. Charact*. **2014,** *31,* 1134-1140.
72. Bastús, N. G.; Comenge, J.; Puntes, V., Kinetically Controlled Seeded Growth Synthesis of Citrate-Stabilized Gold Nanoparticles of up to 200 nm: Size Focusing versus Ostwald Ripening. *Langmuir* **2011,** *27*, 11098-11105.
73. Byers, C. P.; Hoener, B. S.; Chang, W. S.; Yorulmaz, M.; Link, S.; Landes, C. F., Single-Particle Spectroscopy Reveals Heterogeneity in Electrochemical Tuning of the Localized Surface Plasmon. *J. Phys. Chem. B* **2014,** *118*, 14047-14055.